Thermally Activated Octahedral Distortions Generate a Phonon-Assisted Radiative Recombination Pathway in Cubic $CsPbBr_3$ Perovskite Quantum Dots

Vivien L. Cherrette[a], *Finn Babbe*[b], *Jason K. Cooper*[*,b], *and Jin Z. Zhang*[*,a]

[a]*Department of Chemistry and Biochemistry, University of California, Santa Cruz, California 95064, United States*

[b]*Chemical Science Division, Liquid Sunlight Alliance (LiSA), Lawrence Berkeley National Laboratory, Berkeley, California 94720, United States*

Corresponding authors: jkcooper@lbl.gov (J.K.), zhang@ucsc.edu (J. Z.)

TOC Graphic

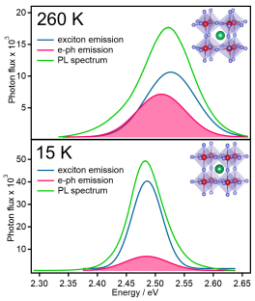

Abstract

Exciton-phonon interactions elucidate structure-function relationships that aid in the control of color purity and carrier diffusion which is necessary for the performance-driven design of solid-state optical emitters. Temperature-dependent steady-state photoluminescence (PL) and time-resolved PL (TRPL) reveal that thermally activated exciton-phonon interactions originate from structural distortions in cubic $CsPbBr_3$ perovskite quantum dots (PQDs) at room temperature. Exciton-phonon interactions cause performance-degrading PL linewidth broadening and slower electron-hole recombination. Structural distortions in cubic PQDs at room temperature exist as octahedral tilting of the $PbBr_6$ subunit. The $PbBr_6$ octahedral distortions cause symmetry breaking, resulting in thermally activated longitudinal optical (LO) phonon coupling to the photoexcited electron-hole pair that manifests as inhomogeneous PL linewidth broadening. At cryogenic temperatures, the linewidth broadening is minimized due to an increase in the cubic phase symmetry of the $PbBr_6$ octahedra. A fundamental understanding of these intrinsic exciton-phonon interactions gives insight into the polymorphic nature of the cubic phase and the origins of performance degradation in PQD optical emitters.All-inorganic $CsPbBr_3$ perovskite quantum dots (PQDs) are a class of solution-processable semiconductor nanocrystals that have gained significant

attention for solid-state lighting and photonics applications due to their facile and low-cost fabrication, tunable optical properties, and near-unity photoluminescence (PL) quantum yields (QY) (>90%).[1–5] Although very promising, PQDs lack in performance in comparison to more mature semiconductors quantum dots (QDs) e.g., II-VI QDs which have narrow emission linewidths and, therefore, are very color pure. PQDs typically have emission linewidths ranging from 70-120 meV at room temperature, while colloidal II-VI QD emission linewidths range between 20-60 meV.[6] Narrow emission is desired for solid-state light-emitting devices and QD displays. We therefore seek to understand the fundamental origins of linewidth broadening in the PL spectrum of PQDs. PL linewidth broadening can originate from several known phenomena including defects, phase impurities, and exciton-phonon coupling.

Structural defects in the core and on the nanocrystalline surface of QDs bring about inhomogeneous linewidth broadening and reduced PL QY efficiency.[7,8] The PL linewidth broadening is due to the development of trap states within the band gap that create low energy emission sidebands. Trap states also generate non-radiative recombination pathways reducing PL QY efficiency. PQDs are more defect tolerant in comparison to typical semiconductor QDs, allowing them to reach relatively high PL QY efficiencies (~70-80%) with low cost and simple synthetic methods.[9] Perovskite defect tolerance is attributed to the large formation energies of vacancies and antisites that cause deep trap states and diminishing PL QY.[10] However, defect formation in PQDs is drastically different from their corresponding bulk materials primarily due to their large surface to volume ratio. The substantial number of uncoordinated surface atoms/ions compared to core atoms/ions often makes surface recombination a primary PL QY loss mechanism. High-quality synthesis methods are necessary to achieve near-unity PL QYs (>90%) and suppress non-radiative recombination. The chemical environment, storage

conditions, and solution temperature can shift the equilibrium away from the ligand passivated surfaces exposing surface defects and causing PL quenching. Incomplete surface passivation can also introduce shallow defects that would contribute to PL linewidth broadening despite achieving relatively high PL QY efficiency.[11,12]

Inhomogeneous PL linewidth broadening can also arise from impurity crystalline phases. The ABX_3 perovskite structure (A= Cs^+, methylammonium (MA^+), formamidinium (FA^+); B= Sn^{2+}, Pb^{2+}; X=Cl^-, Br^-, I^-) consists of a 3D corner-sharing $[BX_6]^{4-}$ octahedral framework with A cations centrally coordinated between. Bulk $CsPbBr_3$ perovskites form monoclinic, orthorhombic, or tetragonal crystalline phases at low temperatures (T < 361 K), while the cubic phase exists at high temperatures (T > 403 K).[13] In contrast, nanocrystals can be stabilized at room temperature in target crystal phases.[14] For example, the room temperature $CsPbBr_3$ nanocrystals were first reported as cubic (*Pm3m*)[9], but reports of tetragonal (*P4/mbm*)[15] and orthorhombic (*Pbnm or Pnma*)[16] phases followed. As each crystal phase has different optoelectronic properties, inhomogeneous PL broadening can result from impurity phases. Yet, even for seemingly high phase-pure nanocrystal, some phase impurities may exist as thermally activated structural distortions known as polymorphous networks.[13,17]

Polymorphous networks that arise from thermal disorder of the lattice can also alter the optical properties. These networks are characterized as the breaking of local symmetry by tilting, rotations, and B-cation displacement.[13] The most common polymorphic network in $CsPbBr_3$ is rigid rotations of the $PbBr_6$ octahedral cages, commonly called octahedral tilting.[18,19] Octahedral tilting breaks the cubic symmetry and can alter the energetics of the band structure.[13] Additionally, octahedral distortions have been known to induce exciton-phonon coupling that causes low energy PL linewidth broadening and slower PL lifetimes.[20–23]

Exciton-phonon interactions can cause linewidth broadening by introducing relaxation pathways for photoexcited carriers causing phonon-assisted sidebands. Longitudinal optical (LO) phonons can only exist in rotationally distorted perovskites, like tetrahedral and orthorhombic, and not in the ideal cubic structures.[21] As such, LO-phonon exciton coupling will emerge in the systems containing octahedral tilting. An examination of the relationship between lattice distortions and exciton-phonon coupling will help gain insight into the structure-function relationships that play a detrimental role on the PL properties.

The monomorphous cubic phase PQDs should have the best color purity compared to other low symmetry phases due to the lack of structural distortions that can cause PL linewidth broadening.[21,24] However, recent studies reveal the accepted monomorphous cubic structure may also undergo polymorphous distortions.[13] To elucidate the true nature of the cubic structure and the origin of PL linewidth broadening, it is necessary to understand exciton-phonon coupling in the PL spectrum.

As phonons are thermally activated, the effects of phonon-assisted recombination pathways are typically studied by low temperature PL and TRPL.[25–27] However, temperature dependent phase transitions makes studying exciton-phonon coupling at low temperature impossible. As mentioned, the temperature dependence of the crystal phases in bulk $CsPbBr_3$ is well recognized: cubic ($T > 403$ K), tetragonal ($403 K > T > 361$ K), and orthorhombic ($T < 361$ K).[17,28–30] To study exciton-phonon coupling in the cubic phase, we have utilized a nanocrystalline system in which the cubic phase is captured during high temperature synthesis and stabilized over all temperature ranges through the use of surface ligands.[14,31]

In this work, homogeneous cubic PQD nanocrystals were synthesized with near-unity PL QY (>90%). We examined these particles by temperature-dependent PL studies between 15 K and

295 K to investigate the relationship between exciton-phonon interactions and structural distortions. We found that cubic PQDs experience polymorphous distortions at room temperature despite being in the pure cubic phase. These distortions cause symmetry breaking that results in thermally activated phonon coupling to the photoexcited exciton that manifests as inhomogeneous PL linewidth broadening. At low temperatures, the inhomogeneous broadening is eliminated due to reduced octahedral tilting and increased monomorphous symmetry.

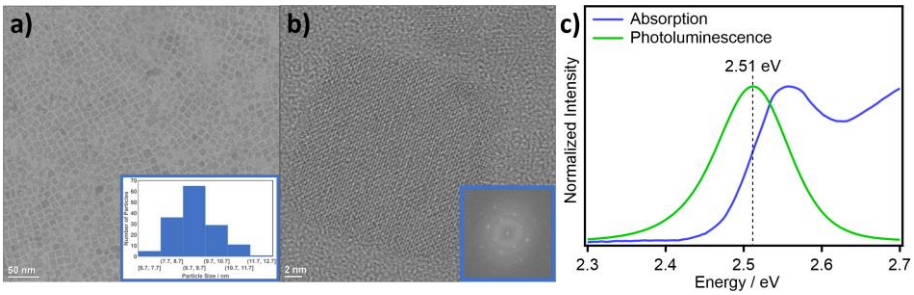

Figure 1 a) HR-TEM of PQDs illustrating monodispersed particle size histogram (inset), b) HR-TEM of single PQD showing cubic crystallinity and fast Fourier transform (FFT) (inset), and c) $CsPbBr_3$ PQD PL and absorption spectrum overlaid and normalized to the corresponding peaks.

Following the well-known hot-injection method, $CsPbBr_3$ PQDs were synthesized at 443 K to form the high temperature cubic phase.[9] High-resolution transmission electron microscopy (HR-TEM) in Figure 1a confirms monodisperse PQDs that are 9.3 ± 0.9 nm in length. Figure 1a inset shows the particle size distribution collected from 150 particles. Figure 1b shows the cubic phase of the single nanocrystal with 4.1 Å d-spacing and the Fourier transform diffraction pattern in the inset. [16,32]

The optical properties of the PQDs were measured in a tetradecane suspension. Aggregation of PQDs can spontaneously occur at lower temperatures and quench PL emission.

The tetradecane freezing point is 278.5 K, which is effective at eliminating PQD aggregation and preserving the PL QY at low temperatures. Figure 1c shows the absorption and PL spectrums at room temperature (293 K). The free exciton absorption energy is 2.56 eV and the PL maximum is at 2.51 eV, indicating a Stoke's shift of 0.05 eV. This binding energy agrees well with previous reports ranging from 38-58 meV.[33,34] Concentration and power dependent studies were conducted to ensure non-linear effects, such as photon recycling, did not play an extended role on PL linewidth broadening as previous reports have found.[35] Figure S1 and S2 in Supporting Information (SI) show that concentration and excitation intensities were well within the linear regime and play a negligible role in the PL linewidth broadening.

The PL spectrum has a full-width half maximum (FWHM) of 110 meV thus showing comparably small spectral broadening on par with previous PQD reports.[6] Fitting of the PL spectrum in Figure S3 reveals inhomogeneous broadening causing red tailing in the emission spectrum; Table S1 in SI provides the Gaussian fit parameters. Two peaks were identified at 2.514 eV, corresponding to the exciton emission, and 2.499 eV, corresponding to the inhomogeneous broadening component. The low energy broadening could arise from a variety of PQD properties including defects, crystal phase impurities, and exciton-phonon interactions. We hypothesize that the low energy tailing in the emission spectrum is caused by exciton-phonon coupling due to octahedral tilting at room temperature. However, the following experiments were done to rule out broadening caused by defects and crystal phase impurities.

Surface defects often reduce PL QY and result in low-energy sidebands that cause inhomogeneous PL linewidth broadening.[36–38] Therefore, to deconvolve phonon interactions in the PL, defects in the PQDs must be negligible. PL QY was calculated using relative methods and compared against perylene dye. The PQDs consistently exhibit PL QY of 91% and are stable for

over a month under an inert atmosphere with no signs of degradation. Table S4 shows the longevity of the PL QYs of the particles in different storage conditions. This near-unity PL QY efficiency suggests the PQDs have excellent surface passivation and minimal defects. Therefore, defect-assisted radiative and non-radiative emission pathways are negligible ensuring efficient charge carrier generation and recombination. [39,40]

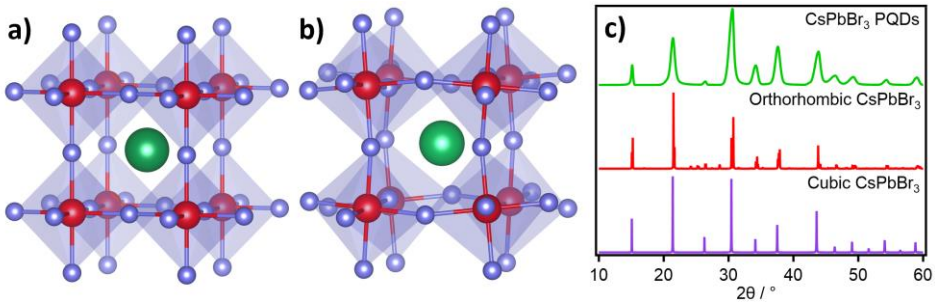

Figure 2 a) Cubic phase perovskite unit cell where the central Cs^+ cation (green) is caged between a corner-sharing $[PbBr_6]^{-4}$ octahedral framework (Pb^{2+}, red/Br^-, purple), b) Orthorhombic phase (not entire unit cell) used to display octahedral tilting of the $PbBr_6$ octahedral cages, and c) XRD spectrum of PQDs (green) showing cubic phase and high crystallinity at room temperature. Theoretical powder XRD spectra for cubic and orthorhombic were calculated in VESTA (COD ID: 1533063 (cubic) and 4510745 (orthorhombic)).[41]

Perovskite nanocrystal syntheses have been known to produce both orthorhombic and cubic phases.[9,16,24,42] To determine crystallinity and crystal phase of the PQDs, we utilized HR-TEM, X-ray diffraction (XRD), and Raman spectroscopy.

The cubic and orthorhombic phases $CsPbBr_3$ are illustrated in Figure 2a,b, where the central Cs^+ cation (green) is caged between a corner-sharing $[PbBr_6]^{-4}$ octahedral framework (Pb^{2+},

red/Br^-, purple). The full orthorhombic unit cell was not used to display octahedral tilting of the $PbBr_6$ octahedral cages. Figure 1b shows the room temperature HR-TEM of a single nanocrystal with cubic symmetry. The measured 4.1 Å d-spacing is in agreement with the expected value 4.15 Å from the {110} cubic plane of the cubic crystal.[41] Additionally, 3.0 Å d-spacing was also observed in good agreement with the expected 2.94 Å of the {200} cubic plane.

The XRD data in Figure 2c agree with cubic symmetry PQDs. However, assigning the crystal phase based only on XRD is challenging due to similar diffraction patterns of the two phases. As such, we employed room temperature Raman scattering to confirm the cubic phase crystals. Orthorhombic and tetragonal structures produce a sharp peak at approximately 105 cm^{-1}, which is absent from the pristine cubic structures.[24] As seen in Figure S2, the PQDs exhibit no significant sharp features and all peaks are attributed to tetradecane solvent. This is typical of perovskite crystals with cubic phase symmetry, as they do not have Raman active modes.[43]

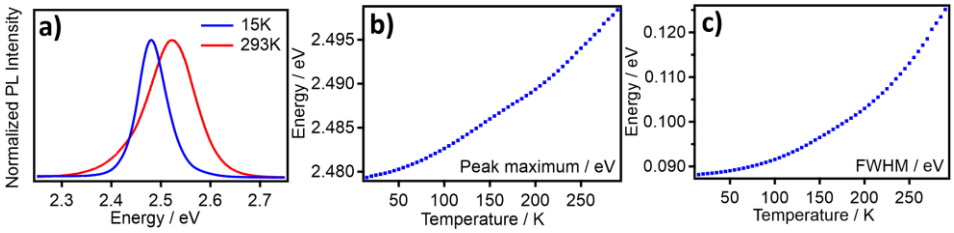

Figure 3 a) Normalized temperature-dependent steady-state PL measured at 15 K and 293 K. PL measurements were taken using a 405 nm pulsed laser and 1800 lines/mm grating for direct comparison to the TRPL. The temperature-dependent PL trend analysis of b) peak position (eV) and c) full-width half maximum (FWHM) (eV). PL trend measurements were taken using a 405 nm continuous wave laser. PL measurements were conducted after allowing the sample to

thermally equilibrate in the dark for 15 minutes. 150 lines/mm grating was used to complete the trend analysis.

We use temperature dependent PL to evaluate the role of exciton-phonon coupling on the PL linewidth broadening. However, temperature dependent phase transitions occur in perovskite bulk material contributing to PL linewidth broadening. As demonstrated in previous studies, the PQD's 0D nanocrystalline surface should stabilize the crystal phase well below the phase transition temperatures expected in the bulk systems.[14] Low-temperature PL experiments were conducted to ensure the crystalline phase remains unchanged for the sole examination of intrinsic exciton-phonon interactions. Temperature-dependent steady-state PL in Figure 3a reveals a blue shift (shift to higher energy) with increasing temperature. The peak shifts from 2.48 eV (15 K) to 2.52 eV (293 K), which indicates the band gap widens with increasing temperature which is consistent with other reports of perovskite materials.[31,36,43] This is atypical of most semiconductors (Si, III-V, II-VI, etc.) that display a red shift, or band gap narrowing, with increasing temperatures due to lattice vibrations that increase the interatomic distance.[44] In PQDs the widening is attributed to the combination of lattice expansion and octahedral tilting.[19]

Lattice expansion and octahedral tilting influence the $CsPbBr_3$ electronic energy levels because of the orbital overlap in the bands. The valence band maximum (VBM) is composed of hybridized antibonding Pb 6s and Br 5p orbitals.[19,45] Lattice expansion and octahedral tilting decrease the Pb-Br overlap which stabilizes the VBM thus, lowering the bands energy. The conduction band maximum (CBM) is composed of Pb 6p non-bonding orbitals. As such, the CBM is less affected by changes in the orbital overlap. The combined effect is a widening of the bandgap at increasing temperature.

Figure 3b shows a gradual shift of the PL peak maximum from 2.48 eV at 15 K to 2.50 eV at 290 K. The gradual progression is characteristic of PQDs as bulk material temperature dependent behavior shows stepwise discontinuities at the phase transition temperatures.[46] The lack of such discontinuities indicate no evidence for first order phase transitions, suggesting the cubic crystal phase is retained from 15-290 K. The retention of cubic crystal symmetry suggests the room temperature PL linewidth broadening is due to exciton-phonon interactions intrinsic to the cubic structure.

The temperature-dependent PL linewidth trend gives insight into exciton-phonon interactions. Figure 3c shows a gradual increase of the linewidth from 88 meV at 15 K to 125 meV at 290 K. Spectral broadening has a combination of homogeneous and inhomogeneous components. Homogeneous broadening at elevated temperature is due to lattice vibrations and has been demonstrated in a variety of solid-state semiconductors including $CsPbBr_3$ bulk, single crystals, and other nanocrystal counterparts.[19,22] The decrease in PL linewidth broadening at 15 K is partly from reducing lattice vibrations. However, we are attributing the inhomogeneous component, manifested as red (low energy) tailing at room temperature, to exciton-phonon coupling that bring about a phonon-assisted emission pathway.

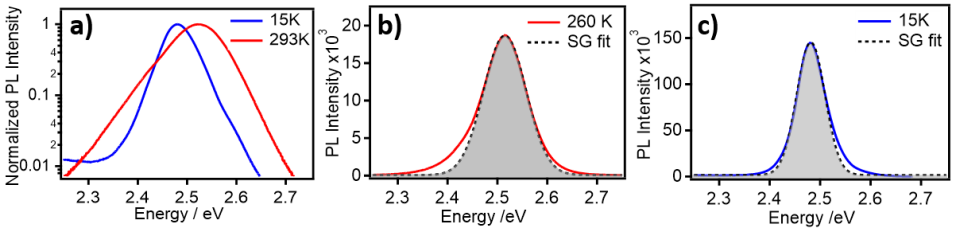

Figure 4 a) Normalized steady-state PL spectra plotted semi-logarithmically show low energy red tail and possible phonon coupling mode. b) 260 K PL fit with single Gaussian (SG). c) 15 K PL fit with SG. PL measurements were conducted under the same conditions as Figure 3a.

Exciton-phonon coupling is thermally activated and close in energy to the exciton manifesting inhomogeneous broadening, or low energy tailing. Low temperature PL studies were further analyzed to observe the inhomogeneous broadening from phonon-assisted emission. Figure 4a displays a semi-logarithmic plot of the PL spectral profile at 15 K and 293 K to better express the temperature-dependence of the low energy tailing. The room temperature tailing is shown by a non-Gaussian low energy shoulder that diminishes at 15 K. The shoulder is not discrete, supporting that the low energy tailing is close in energy to the exciton emission. Furthermore, both measurements were fit with a single Gaussian (SG) fit function displayed in Figures 4b,c. The shaded SG fits show the disappearance of the low energy tailing at 15 K. The gradual disappearance of the low energy tailing is also seen at 130 and 170 K in Figure S5.

Previous literature reports the opposite for perovskite nanocrystals in terms of low energy tailing or even the appearance of a discrete peak at low temperatures.[21,24,36,47] The peak at low temperatures is attributed to carriers recombining through a phonon-assisted emission pathway. This phonon-assisted emission correlates to locked structural distortions of the orthorhombic crystal phase.[21] In the case of this study, the low energy tailing only occurs at elevated temperatures

and disappears at 15 K. This suggests the phonon-assisted emission pathway is due to thermally induced structural distortions. The lack of low-energy sidebands at 15 K also confirms the PQDs are cubic, and not orthorhombic. TRPL kinetics studies are needed to confirm the presence of the two emission pathways at room temperature: 1) exciton recombination and 2) phonon-assisted recombination.

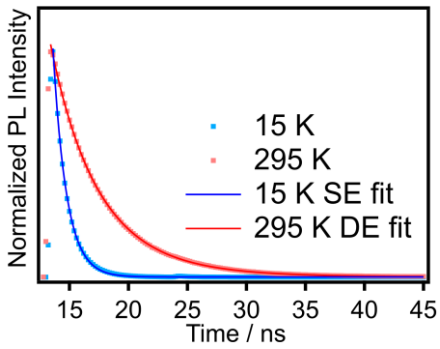

Figure 5 Time-resolved PL at 15 K (raw data, blue dots, and single exponential (SE) fit, blue line) and 295 K (raw data, red dots, and double exponential (DE) fit, red line). TRPL measurements were conducted under the same conditions as Figure 3a.

In efforts to resolve the thermally activated phonon-assisted emission pathway, TRPL was utilized to verify the presence of multiple radiative recombination pathways buried within the PL spectrum. Figure 5 depicts TRPL behavior at 15 K and 295 K. At 295 K, the PL decay time was best fit using a double exponential (DE) function. The 15 K had best fit agreement with a single exponential (SE) function. The biexponential character at room temperature verified the presence of two emission pathways, while the more single exponential character at 15 K verified the presence of one dominant emission pathway. The disappearance of one emission pathway at 15 K

suggests that there is indeed a thermally activated emission pathway generated at room temperature.

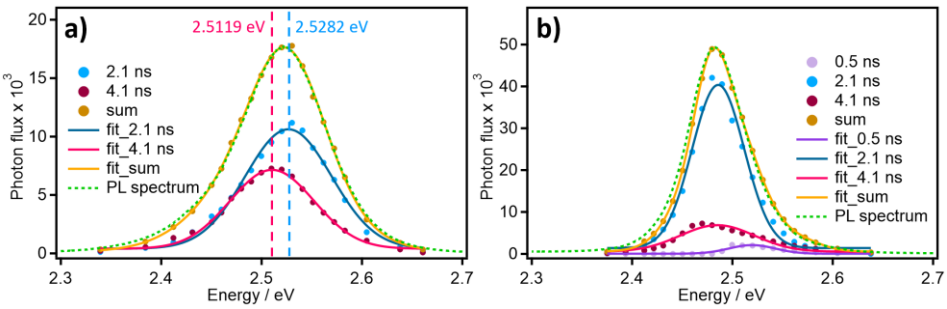

Figure 6 Energy-dependent time-resolved PL spectra at a) 260 K and b) 15 K. Tetradecane PQD suspensions are frozen from 15-260 K to ensure QD aggregation is minimized. PL and TRPL measurements were conducted under the same conditions as Figure 3a.

Further resolution of the discrete energy levels of the exciton emission and the alternate thermally activated emission pathways are necessary to reveal an exciton-phonon coupling mode that can be structurally assigned. Energy-dependent TRPL experiments at 15 K and 260 K displayed in Figure 6 were conducted to resolve the discrete energies of multiple emission pathways. These experiments were carried out by measuring the TRPL at several monochromator wavelengths. The exponential decays at 260 K in Figure 6a were best fit with PL decay times held constant at 2.1 ns and 4.1 ns. These PL decay times are consistent with PL lifetimes previously observed in literature.[48] After fitting the respective PL exponential decay amplitudes, the presence of two energy states at 260 K, 2.5119 eV and 2.5282 eV, were resolved. The sum of these energy states was overlaid with the steady-state PL spectrum to confirm proper fitting parameters and excellent agreement. The high energy state at 2.5282 eV with a 2.1 ns PL decay time is assigned as the

exciton emission pathway. The low energy state at 2.5119 eV with a 4.1 ns PL decay time pertains to the thermally activated emission pathway that is causing PL linewidth broadening at room temperature. The low energy thermally activated emission pathway has a longer decay time than the exciton emission verifying that the thermally activated alternate emission pathway is the sole contributor to longer PL decay times. In comparison, the 15 K spectrum in Figure 6b shows the disappearance of the thermally activated emission pathway (red fit) and the narrowing of the PL linewidth. The gradual disappearance of this phonon mode is observed at 130 and 170 K in Figure S6. As the thermal energy decreases, it is expected that phonon-assisted recombination would decrease as well. There is an additional fast component, 0.5 ns, for the PL monitored at approximately 2.52 eV. This fast process may be attributed to biexciton Auger recombination.[49]

At room temperature, the energy difference between the discrete states is 16.3 meV (131.5 cm^{-1}). At 15 K, the low energy tailing component decreases in intensity and the exciton-phonon coupling mode is diminishes. The energy difference that appears at room temperature suggests the formation of a thermally activated vibrational mode in agreement with the LO phonon energy (20 meV) calculated in Figure S7. The 131.5 cm^{-1} vibrational mode is correlated to the transverse and LO phonon modes due to Pb-Br stretching vibrations in the octahedra.[27] A theoretical Raman study of lead-based perovskite single crystals identifies these optical phonon modes as the asymmetric (127 cm^{-1}) and symmetric (147 cm^{-1}) bending modes of the Pb-Br octahedra.[23] However, these modes are only observed in PQDs with orthorhombic crystal symmetry at low temperatures.[22] This suggests that the cubic polymorphs are thermally induced octahedral distortions that generate a phonon-assisted emission pathway inducing PL linewidth broadening at room temperature. In summary, we demonstrated that PQD cubic phase still exhibits an inhomogeneous PL linewidth broadening and longer PL lifetimes due to thermally activated phonon coupling to the exciton.

This exciton-phonon coupling can be explained by $PbBr_6$ octahedral tilting that occurs at room temperature and pertains to the LO phonon energy (20 meV). At 15 K, the phonon-assisted radiative recombination pathway is largely mitigated as manifested by pure excitonic emission with minimal phonon-assisted emission. This suggests that the $PbBr_6$ octahedral distortions are minimized, and octahedral symmetry of the cubic phase is locked. Although the cubic phase PQDs are stabilized over a broad range of temperatures (15-300 K), it still experiences some low symmetry octahedral distortions at room temperature. These distortions at room temperature confirm the cubic phase polymorphous networks are thermally induced. Understanding of the exciton-phonon coupling is an important step toward the rational design of high-performing, color pure optical emitters for photonics application including solid-state lighting.*Materials*

Cesium carbonate (99.99%, Sigma Aldrich), lead bromide (99.99%, Alfa Aezar), octadecene (90%, Sigma Aldrich), oleic acid (90% tech grade, Sigma Aldrich), and 70% tech grade oleylamine (Sigma Aldrich). 70% tech grade oleylamine was purified using purifications method by Baranov et al.[50]

Preparation of Cs-oleate precursor

0.40 g Cs_2CO_3 was loaded into a 50 mL 3-neck flask along with 18 mL octadecene (ODE), 90%, and 2.5 mL oleic acid (OA), 90%. Cs_2CO_3 is hygroscopic and was stored and weighed out in a N_2 glove box. This solution was dried under vacuum for 1 hour at 120˚C. The flask was then purged with N_2 and heated to 150 ˚C until all Cs_2CO_3 was reacted with oleic acid (about 5-10 minutes). The final solution is clear and translucent with a yellow tint when heated above 100˚C.

Since Cs-oleate precipitates out of ODE at room-temperature, it was pre-heated to 115˚C before injection.

Synthesis of CsPbBr3 perovskite quantum dots

0.188 mmol (0.069 g) of $PbBr_2$ was loaded into a 25 mL 3-neck round-bottom flask with 5.0 mL of ODE. The solution was dried under vacuum with stirring for 1 hour (ramp up to 120˚C in 30 mins (4˚C/min)). The flask was then purged with N_2 and 0.5 mL dried oleylamine (OAm) and 0.50 mL dried oleic acid (OA) where injected at 120˚C. After complete solubilization of $PbBr_2$ salt, the precursor solution was heated to 170˚C. Cs-oleate precursor was heated to 115˚C for clear yellow solution. 0.40 mL (0.125M) of hot Cs-oleate was swiftly injected into $PbBr_2$ solution and reacted for 1 minute with stirring (1000 rpm). After, the reaction was immediately cooled in an ice water bath.

The crude solution was transferred into a 15 mL polypropylene centrifuge tube and centrifuge at 10,000 rpm for three minutes. The supernatant was discarded, and the resulting pellet was redisperse in 600 µL of tetradecane by shaking (Supernatant should luminescence blue under UV light indicating formation of smaller particles). The suspension was then centrifuged at 10,000 rpm for 3 minutes. The quantum dots within the supernatant were kept and the pellet discarded. The resulting supernatant was diluted with 3.6 mL of tetradecane. The PL spectral profiles of 260 K and 15 K were collected to ensure the sample was solidified for both measurements since 260 K is well below the freezing point temperature of tetradecane.

PLQY methods

Relative PLQY was measured via a custom built PLQY system equipped with a UV white light source, a 405 nm LED light source, and a spectrometer to sequentially observe the transmission and emission spectrum of the nanoparticles. We calculated PLQY using Equation 1 and compared against a perylene dye standard.

$$\Phi_X = \Phi_{ST}\left(\frac{Grad_X}{Grad_{ST}}\right)\left(\frac{\eta_X{}^2}{\eta_{ST}{}^2}\right) \quad \text{Equation 1}$$

HR-TEM

High-resolution transmission electron microscopy (HRTEM) was performed on a FEI UT Tecnai microscope operated at 200 kV acceleration voltage. Diameter measurements were taken directly from the electron microscopy images by using ImageJ software. For each sample, 150 PQD lengths were used to calculate the average diameter of 9+/-1 nm.

XRD

X-ray diffraction (XRD) was performed on a Rigaku diffractometer operated in BB mode (10 mm) with κβ filter. Diffraction patterns were analyzed using Smart Lab studio II software.

Steady-state PL methods

Steady-state PL measurements were taken using a 405 nm pulsed wave laser (~0.9 µW average power) for direct comparison to the TRPL. The Andor Technology Step and Glue function was utilized to collect the entirety of the high-resolution spectrum with an 1800 lines/mm grating and 1000 µm slit width.

PL trend measurements were taken using a 405 nm continuous wave source (7 mW), a 150 lines/mm grating, and 1000 µm slit width. All PL measurements were taken and analyzed using Andor Software:Solis. Each measurement was automated in LabView and held for 15 minute to ensure thermal equilibrium.

There is an offset in room temperature trend values for peak maximum (MS Figure 3b, 2.50 eV) in comparison to the previous PL measurements (MS Figure 3a, 2.52 meV), which used

a higher resolution grating, however, the trend is unaffected by this parameter. The origin of inconsistency is dependent on instrumental calibration such as grating resolution and slit width.

Time-resolved PL methods (Energy-dependent TRPL methods)

TRPL measurements were measured using time-correlated single photon counting (Micron photon device) and analyzed using Timeharp 260 software. The measurements were taken using a 405 nm pulsed wave source (~0.9 µW average power), a 1800 lines/mm grating, 0.2 ns resolutions, and 1000 µm input slit width/100 µm output slit width. Slit widths were calibrated to ensure proper overlay between steady-state and time-resolved PL spectrums. Calibrations depicted in Figure S9. Illumination studies were executed to ensure samples were stable under continuous and pulsed illumination for a 16-hour period.

Supporting Information. Contains supplementary content on PQD PL QY stability measurements, Raman spectra of PQDs, accompanying PL/TRPL temperature data for 130 and 170 K, FWHM fitting model equation, and output slit width and grating resolution calibration.Corresponding Authors

*E-mail: jkcooper@lbl.gov

*E-mail: zhang@ucsc.edu

Notes

The authors declare no competing financial interest.

This material is based upon work supported by the U.S. Department of Energy, Office of Science, Office of Workforce Development for Teachers and Scientists, Office of Science Graduate Student Research (SCGSR) program. The SCGSR program is administered by the Oak Ridge Institute for Science and Education (ORISE) for the DOE. ORISE is managed by ORAU under contract number DE-SC0014664. All opinions expressed in this paper are the author's and do not necessarily reflect the policies and views of DOE, ORAU, or

Formatted: German (Germany)
Formatted: German (Germany)
Formatted: German (Germany)
Field Code Changed
Field Code Changed
Formatted: English (United States)

ORISE. VLC is grateful to the Liquid Sunlight Alliance (LiSA) at Lawrence Berkeley National Laboratory (LBNL) for the use of their B30 facilities. VLC acknowledges the support in data analysis from Sayantani Ghosh, UC Merced, and Jeremy Barnett, UCSC. FB and JC acknowledge support from the U.S. Department of Energy, Office of Science, Office of Basic Energy Sciences, Fuels from Sunlight Hub under Award Number DE-SC0021266. Zhang lab at UCSC is grateful to the US NSF for financial support (CHE-1904547 and CHE-2203633). We would like to acknowledge the Molecular Foundry National Center of Electron Microscopy (NCEM) at LBNL for the HR-TEM.

(1) Akkerman, Q. A.; Rainò, G.; Kovalenko, M. V.; Manna, L. Genesis, Challenges and Opportunities for Colloidal Lead Halide Perovskite Nanocrystals. *Nat. Mater.* **2018**, *17* (5), 394–405. https://doi.org/10.1038/s41563-018-0018-4.

(2) Dey, A.; Ye, J.; De, A.; Debroye, E.; Ha, S. K.; Bladt, E.; Kshirsagar, A. S.; Wang, Z.; Yin, J.; Wang, Y.; Quan, L. N.; Yan, F.; Gao, M.; Li, X.; Shamsi, J.; Debnath, T.; Cao, M.; Scheel, M. A.; Kumar, S.; Steele, J. A.; Gerhard, M.; Chouhan, L.; Xu, K.; Wu, X.; Li, Y.; Zhang, Y.; Dutta, A.; Han, C.; Vincon, I.; Rogach, A. L.; Nag, A.; Samanta, A.; Korgel, B. A.; Shih, C.-J.; Gamelin, D. R.; Son, D. H.; Zeng, H.; Zhong, H.; Sun, H.; Demir, H. V.; Scheblykin, I. G.; Mora-Seró, I.; Stolarczyk, J. K.; Zhang, J. Z.; Feldmann, J.; Hofkens, J.; Luther, J. M.; Pérez-Prieto, J.; Li, L.; Manna, L.; Bodnarchuk, M. I.; Kovalenko, M. V.; Roeffaers, M. B. J.; Pradhan, N.; Mohammed, O. F.; Bakr, O. M.; Yang, P.; Müller-Buschbaum, P.; Kamat, P. V.; Bao, Q.; Zhang, Q.; Krahne, R.; Galian, R. E.; Stranks, S. D.; Bals, S.; Biju, V.; Tisdale, W. A.; Yan, Y.; Hoye, R. L. Z.; Polavarapu, L. State of the Art and Prospects for Halide Perovskite Nanocrystals. *ACS Nano* **2021**, *15* (7), 10775–10981. https://doi.org/10.1021/acsnano.0c08903.

(3) Zhang, Q.; Shang, Q.; Su, R.; Do, T. T. H.; Xiong, Q. Halide Perovskite Semiconductor Lasers: Materials, Cavity Design, and Low Threshold. *Nano Lett.* **2021**, *21* (5), 1903–1914. https://doi.org/10.1021/acs.nanolett.0c03593.

(4) Liu, M.; Grandhi, G. K.; Matta, S.; Mokurala, K.; Litvin, A.; Russo, S.; Vivo, P. Halide Perovskite Nanocrystal Emitters. *Adv. Photonics Res.* **2021**, *2* (3), 2000118. https://doi.org/10.1002/adpr.202000118.

(5) Wang, Y.; Li, X.; Song, J.; Xiao, L.; Zeng, H.; Sun, H. All-Inorganic Colloidal Perovskite Quantum Dots: A New Class of Lasing Materials with Favorable Characteristics. *Adv. Mater.* **2015**, *27* (44), 7101–7108. https://doi.org/10.1002/adma.201503573.

(6) Rainò, G.; Yazdani, N.; Boehme, S. C.; Kober-Czerny, M.; Zhu, C.; Krieg, F.; Rossell, M. D.; Erni, R.; Wood, V.; Infante, I.; Kovalenko, M. V. Ultra-Narrow Room-Temperature Emission from Single CsPbBr3 Perovskite Quantum Dots. *Nat. Commun.* **2022**, *13* (1), 2587. https://doi.org/10.1038/s41467-022-30016-0.

(7) Janke, E. M.; Williams, N. E.; She, C.; Zherebetskyy, D.; Hudson, M. H.; Wang, L.; Gosztola, D. J.; Schaller, R. D.; Lee, B.; Sun, C.; Engel, G. S.; Talapin, D. V. Origin of Broad Emission Spectra in InP Quantum Dots: Contributions from Structural and Electronic Disorder. *J. Am. Chem. Soc.* **2018**, *140* (46), 15791–15803. https://doi.org/10.1021/jacs.8b08753.

(8) Cho, E.; Kim, T.; Choi, S.; Jang, H.; Min, K.; Jang, E. Optical Characteristics of the Surface Defects in InP Colloidal Quantum Dots for Highly Efficient Light-Emitting Applications. *ACS Appl. Nano Mater.* **2018**, *1* (12), 7106–7114. https://doi.org/10.1021/acsanm.8b01947.

(9) Protesescu, L.; Yakunin, S.; Bodnarchuk, M. I.; Krieg, F.; Caputo, R.; Hendon, C. H.; Yang, R. X.; Walsh, A.; Kovalenko, M. V. Nanocrystals of Cesium Lead Halide Perovskites ($CsPbX_3$, X = Cl, Br, and I): Novel Optoelectronic Materials Showing Bright Emission with Wide Color Gamut. *Nano Lett.* **2015**, *15* (6), 3692–3696. https://doi.org/10.1021/nl5048779.
(10) ten Brinck, S.; Zaccaria, F.; Infante, I. Defects in Lead Halide Perovskite Nanocrystals: Analogies and (Many) Differences with the Bulk. *ACS Energy Lett.* **2019**, *4* (11), 2739–2747. https://doi.org/10.1021/acsenergylett.9b01945.
(11) Li, J.; Yuan, X.; Jing, P.; Li, J.; Wei, M.; Hua, J.; Zhao, J.; Tian, L. Temperature-Dependent Photoluminescence of Inorganic Perovskite Nanocrystal Films. *RSC Adv.* **2016**, *6* (82), 78311–78316. https://doi.org/10.1039/C6RA17008K.
(12) Lee, S. M.; Moon, C. J.; Lim, H.; Lee, Y.; Choi, M. Y.; Bang, J. Temperature-Dependent Photoluminescence of Cesium Lead Halide Perovskite Quantum Dots: Splitting of the Photoluminescence Peaks of $CsPbBr_3$ and $CsPb(Br/I)_3$ Quantum Dots at Low Temperature. *J. Phys. Chem. C* **2017**, *121* (46), 26054–26062. https://doi.org/10.1021/acs.jpcc.7b06301.
(13) Zhao, X.-G.; Dalpian, G. M.; Wang, Z.; Zunger, A. Polymorphous Nature of Cubic Halide Perovskites. *Phys. Rev. B* **2020**, *101* (15), 155137. https://doi.org/10.1103/PhysRevB.101.155137.
(14) Swarnkar, A.; Marshall, A. R.; Sanehira, E. M.; Chernomordik, B. D.; Moore, D. T.; Christians, J. A.; Chakrabarti, T.; Luther, J. M. Quantum Dot–Induced Phase Stabilization of α-$CsPbI_3$ Perovskite for High-Efficiency Photovoltaics. *Science* **2016**, *354* (6308), 92–95. https://doi.org/10.1126/science.aag2700.
(15) Sercel, P. C.; Lyons, J. L.; Wickramaratne, D.; Vaxenburg, R.; Bernstein, N.; Efros, A. L. Exciton Fine Structure in Perovskite Nanocrystals. *Nano Lett.* **2019**, *19* (6), 4068–4077. https://doi.org/10.1021/acs.nanolett.9b01467.
(16) Cottingham, P.; Brutchey, R. L. On the Crystal Structure of Colloidally Prepared $CsPbBr_3$ Quantum Dots. *Chem. Commun.* **2016**, *52* (30), 5246–5249. https://doi.org/10.1039/C6CC01088A.
(17) Whitcher, T. J.; Gomes, L. C.; Zhao, D.; Bosman, M.; Chi, X.; Wang, Y.; Carvalho, A.; Hui, H. K.; Chang, Q.; Breese, M. B. H.; Castro Neto, A. H.; Wee, A. T. S.; Sun, H. D.; Chia, E. E. M.; Rusydi, A. Dual Phases of Crystalline and Electronic Structures in the Nanocrystalline Perovskite CsPbBr3. *NPG Asia Mater.* **2019**, *11* (1), 70. https://doi.org/10.1038/s41427-019-0170-6.
(18) Fu, Y.; Jiang, X.; Li, X.; Traore, B.; Spanopoulos, I.; Katan, C.; Even, J.; Kanatzidis, M. G.; Harel, E. Cation Engineering in Two-Dimensional Ruddlesden–Popper Lead Iodide Perovskites with Mixed Large A-Site Cations in the Cages. *J. Am. Chem. Soc.* **2020**, *142* (8), 4008–4021. https://doi.org/10.1021/jacs.9b13587.
(19) Prasanna, R.; Gold-Parker, A.; Leijtens, T.; Conings, B.; Babayigit, A.; Boyen, H.-G.; Toney, M. F.; McGehee, M. D. Band Gap Tuning via Lattice Contraction and Octahedral Tilting in Perovskite Materials for Photovoltaics. *J. Am. Chem. Soc.* **2017**, *139* (32), 11117–11124. https://doi.org/10.1021/jacs.7b04981.
(20) Fabini, D. H.; Laurita, G.; Bechtel, J. S.; Stoumpos, C. C.; Evans, H. A.; Kontos, A. G.; Raptis, Y. S.; Falaras, P.; Van der Ven, A.; Kanatzidis, M. G.; Seshadri, R. Dynamic Stereochemical Activity of the Sn^{2+} Lone Pair in Perovskite $CsSnBr_3$. *J. Am. Chem. Soc.* **2016**, *138* (36), 11820–11832. https://doi.org/10.1021/jacs.6b06287.

(21) Iaru, C. M.; Geuchies, J. J.; Koenraad, P. M.; Vanmaekelbergh, D.; Silov, A. Yu. Strong Carrier–Phonon Coupling in Lead Halide Perovskite Nanocrystals. *ACS Nano* **2017**, *11* (11), 11024–11030. https://doi.org/10.1021/acsnano.7b05033.
(22) Huang, X.; Li, X.; Tao, Y.; Guo, S.; Gu, J.; Hong, H.; Yao, Y.; Guan, Y.; Gao, Y.; Li, C.; Lü, X.; Fu, Y. Understanding Electron–Phonon Interactions in 3D Lead Halide Perovskites from the Stereochemical Expression of 6s ^{2} Lone Pairs. *J. Am. Chem. Soc.* **2022**, *144* (27), 12247–12260. https://doi.org/10.1021/jacs.2c03443.
(23) Naqvi, F. H.; Ko, J.-H.; Kim, T. H.; Ahn, C. W.; Hwang, Y.; Sheraz, M.; Kim, S. A-Site Cation Effect on Optical Phonon Modes and Thermal Stability in Lead-Based Perovskite Bromide Single Crystals Using Raman Spectroscopy. *J. Korean Phys. Soc.* **2022**, *81* (3), 230–240. https://doi.org/10.1007/s40042-022-00505-y.
(24) Sarang, S.; Bonabi Naghadeh, S.; Luo, B.; Kumar, P.; Betady, E.; Tung, V.; Scheibner, M.; Zhang, J. Z.; Ghosh, S. Stabilization of the Cubic Crystalline Phase in Organometal Halide Perovskite Quantum Dots via Surface Energy Manipulation. *J. Phys. Chem. Lett.* **2017**, *8* (21), 5378–5384. https://doi.org/10.1021/acs.jpclett.7b02399.
(25) Wright, A. D.; Verdi, C.; Milot, R. L.; Eperon, G. E.; Pérez-Osorio, M. A.; Snaith, H. J.; Giustino, F.; Johnston, M. B.; Herz, L. M. Electron–Phonon Coupling in Hybrid Lead Halide Perovskites. *Nat. Commun.* **2016**, *7* (1), 11755. https://doi.org/10.1038/ncomms11755.
(26) Lao, X.; Yang, Z.; Su, Z.; Bao, Y.; Zhang, J.; Wang, X.; Cui, X.; Wang, M.; Yao, X.; Xu, S. Anomalous Temperature-Dependent Exciton–Phonon Coupling in Cesium Lead Bromide Perovskite Nanosheets. *J. Phys. Chem. C* **2019**, *123* (8), 5128–5135. https://doi.org/10.1021/acs.jpcc.9b00091.
(27) Zhao, Z.; Zhong, M.; Zhou, W.; Peng, Y.; Yin, Y.; Tang, D.; Zou, B. Simultaneous Triplet Exciton–Phonon and Exciton–Photon Photoluminescence in the Individual Weak Confinement $CsPbBr_3$ Micro/Nanowires. *J. Phys. Chem. C* **2019**, *123* (41), 25349–25358. https://doi.org/10.1021/acs.jpcc.9b06643.
(28) Hirotsu, S.; Harada, J.; Iizumi, M.; Gesi, K. Structural Phase Transitions in $CsPbBr_3$. *J. Phys. Soc. Jpn.* **1974**, *37* (5), 1393–1398. https://doi.org/10.1143/JPSJ.37.1393.
(29) Mannino, G.; Deretzis, I.; Smecca, E.; La Magna, A.; Alberti, A.; Ceratti, D.; Cahen, D. Temperature-Dependent Optical Band Gap in $CsPbBr_3$, $MAPbBr_3$, and $FAPbBr_3$ Single Crystals. *J. Phys. Chem. Lett.* **2020**, *11* (7), 2490–2496. https://doi.org/10.1021/acs.jpclett.0c00295.
(30) He, Y.; Matei, L.; Jung, H. J.; McCall, K. M.; Chen, M.; Stoumpos, C. C.; Liu, Z.; Peters, J. A.; Chung, D. Y.; Wessels, B. W.; Wasielewski, M. R.; Dravid, V. P.; Burger, A.; Kanatzidis, M. G. High Spectral Resolution of Gamma-Rays at Room Temperature by Perovskite CsPbBr3 Single Crystals. *Nat. Commun.* **2018**, *9* (1), 1609. https://doi.org/10.1038/s41467-018-04073-3.
(31) Diroll, B. T.; Zhou, H.; Schaller, R. D. Low-Temperature Absorption, Photoluminescence, and Lifetime of $CsPbX_3$ (X = Cl, Br, I) Nanocrystals. *Adv. Funct. Mater.* **2018**, *28* (30), 1800945. https://doi.org/10.1002/adfm.201800945.
(32) Brennan, M. C.; Kuno, M.; Rouvimov, S. Crystal Structure of Individual $CsPbBr_3$ Perovskite Nanocubes. *Inorg. Chem.* **2019**, *58* (2), 1555–1560. https://doi.org/10.1021/acs.inorgchem.8b03078.

(33) Zhang, Q.; Su, R.; Liu, X.; Xing, J.; Sum, T. C.; Xiong, Q. High-Quality Whispering-Gallery-Mode Lasing from Cesium Lead Halide Perovskite Nanoplatelets. *Adv. Funct. Mater.* **2016**, *26* (34), 6238–6245. https://doi.org/10.1002/adfm.201601690.
(34) Qaid, S. M. H.; Ghaithan, H. M.; Al-Asbahi, B. A.; Aldwayyan, A. S. Achieving Optical Gain of the $CsPbBr_3$ Perovskite Quantum Dots and Influence of the Variable Stripe Length Method. *ACS Omega* **2021**, *6* (8), 5297–5309. https://doi.org/10.1021/acsomega.0c05414.
(35) Giovanni, D.; Righetto, M.; Zhang, Q.; Lim, J. W. M.; Ramesh, S.; Sum, T. C. Origins of the Long-Range Exciton Diffusion in Perovskite Nanocrystal Films: Photon Recycling vs Exciton Hopping. *Light Sci. Appl.* **2021**, *10* (1), 2. https://doi.org/10.1038/s41377-020-00443-z.
(36) Li, J.; Yuan, X.; Jing, P.; Li, J.; Wei, M.; Hua, J.; Zhao, J.; Tian, L. Temperature-Dependent Photoluminescence of Inorganic Perovskite Nanocrystal Films. *RSC Adv.* **2016**, *6* (82), 78311–78316. https://doi.org/10.1039/C6RA17008K.
(37) Aceves, R.; Babin, V.; Flores, M. B.; Fabeni, P.; Maaroos, A.; Nikl, M.; Nitsch, K.; Pazzi, G. P.; Salas, R. P.; Sildos, I.; Zazubovich, N.; Zazubovich, S. Spectroscopy of CsPbBr3 Quantum Dots in CsBr:Pb Crystals. *J. Lumin.* **2001**, *93* (1), 27–41. https://doi.org/10.1016/S0022-2313(01)00175-2.
(38) Nikl, M.; Nitsch, K.; Mihóková, E.; Polák, K.; Fabeni, P.; Pazzi, G. P.; Gurioli, M.; Santucci, S.; Phani, R.; Scacco, A.; Somma, F. Luminescence of CsPbBr3-like Quantum Dots in CsBr Single Crystals. *Phys. E Low-Dimens. Syst. Nanostructures* **1999**, *4* (4), 323–331. https://doi.org/10.1016/S1386-9477(99)00016-8.
(39) Kim, Y.-H.; Kim, S.; Kakekhani, A.; Park, J.; Park, J.; Lee, Y.-H.; Xu, H.; Nagane, S.; Wexler, R. B.; Kim, D.-H.; Jo, S. H.; Martínez-Sarti, L.; Tan, P.; Sadhanala, A.; Park, G.-S.; Kim, Y.-W.; Hu, B.; Bolink, H. J.; Yoo, S.; Friend, R. H.; Rappe, A. M.; Lee, T.-W. Comprehensive Defect Suppression in Perovskite Nanocrystals for High-Efficiency Light-Emitting Diodes. *Nat. Photonics* **2021**, *15* (2), 148–155. https://doi.org/10.1038/s41566-020-00732-4.
(40) Utzat, H.; Sun, W.; Kaplan, A. E. K.; Krieg, F.; Ginterseder, M.; Spokoyny, B.; Klein, N. D.; Shulenberger, K. E.; Perkinson, C. F.; Kovalenko, M. V.; Bawendi, M. G. Coherent Single-Photon Emission from Colloidal Lead Halide Perovskite Quantum Dots. *Science* **2019**, *363* (6431), 1068–1072. https://doi.org/10.1126/science.aau7392.
(41) Koichi Momma; Fujio Izumi. VESTA, 2011.
(42) Zhang, D.; Eaton, S. W.; Yu, Y.; Dou, L.; Yang, P. Solution-Phase Synthesis of Cesium Lead Halide Perovskite Nanowires. *J. Am. Chem. Soc.* **2015**, *137* (29), 9230–9233. https://doi.org/10.1021/jacs.5b05404.
(43) Ledinsky, M.; Schönfeldová, T.; Holovský, J.; Aydin, E.; Hájková, Z.; Landová, L.; Neyková, N.; Fejfar, A.; De Wolf, S. Temperature Dependence of the Urbach Energy in Lead Iodide Perovskites. *J. Phys. Chem. Lett.* **2019**, *10* (6), 1368–1373. https://doi.org/10.1021/acs.jpclett.9b00138.
(44) Klingshirn, C. F. *Semiconductor Optics*; Graduate Texts in Physics; Springer Berlin Heidelberg: Berlin, Heidelberg, 2012. https://doi.org/10.1007/978-3-642-28362-8.
(45) Xie, Y.; Peng, B.; Bravić, I.; Yu, Y.; Dong, Y.; Liang, R.; Ou, Q.; Monserrat, B.; Zhang, S. Highly Efficient Blue-Emitting $CsPbBr_3$ Perovskite Nanocrystals through Neodymium Doping. *Adv. Sci.* **2020**, *7* (20), 2001698. https://doi.org/10.1002/advs.202001698.

(46) Thomson, S. Observing Phase Transitions in a Halide Perovskite Using Temperature Dependent Photoluminescence Spectroscopy, 2018. https://www.edinst.com/wp-content/uploads/2018/05/AN45_Phase-Transitions_Halide-Perovskites.pdf.
(47) Lee, S. M.; Moon, C. J.; Lim, H.; Lee, Y.; Choi, M. Y.; Bang, J. Temperature-Dependent Photoluminescence of Cesium Lead Halide Perovskite Quantum Dots: Splitting of the Photoluminescence Peaks of $CsPbBr_3$ and $CsPb(Br/I)_3$ Quantum Dots at Low Temperature. *J. Phys. Chem. C* **2017**, *121* (46), 26054–26062. https://doi.org/10.1021/acs.jpcc.7b06301.
(48) Chen, H.; Guo, A.; Zhu, J.; Cheng, L.; Wang, Q. Tunable Photoluminescence of CsPbBr3 Perovskite Quantum Dots for Their Physical Research. *Appl. Surf. Sci.* **2019**, *465*, 656–664. https://doi.org/10.1016/j.apsusc.2018.08.211.
(49) Makarov, N. S.; Guo, S.; Isaienko, O.; Liu, W.; Robel, I.; Klimov, V. I. Spectral and Dynamical Properties of Single Excitons, Biexcitons, and Trions in Cesium–Lead-Halide Perovskite Quantum Dots. *Nano Lett.* **2016**, *16* (4), 2349–2362. https://doi.org/10.1021/acs.nanolett.5b05077.
(50) Baranov, D.; Lynch, M. J.; Curtis, A. C.; Carollo, A. R.; Douglass, C. R.; Mateo-Tejada, A. M.; Jonas, D. M. Purification of Oleylamine for Materials Synthesis and Spectroscopic Diagnostics for *Trans* Isomers. *Chem. Mater.* **2019**, *31* (4), 1223–1230. https://doi.org/10.1021/acs.chemmater.8b04198.